Structure Evolution and Thermal Decomposition of Supramolecular and Lamellar Hybrid Sulfates Templated by 4-Aminopyridinium

Nabil Hfidhi, Omar Kammoun, Thierry Bataille, Houcine Naili

Structure evolution and thermal decomposition of supramolecular and lamellar hybrid sulfates templated by 4-aminopyridinium

Nabil Hfidhi[a], Omar Kammoun[a], Thierry Bataille[b] and Houcine Naïli[a]*

[a]Laboratoire Physico-chimie de l'Etat Solide, Département de Chimie, Faculté des Sciences de Sfax, B.P. 1171, 3000 Sfax, Université de Sfax, Tunisie.

[b]Univ Rennes, Ecole Nationale Supérieure de Chimie de Rennes, CNRS, ISCR - UMR 6226, F- 35000 Rennes, France.

Corresponding author: houcine_naili@yahoo.com

Abstract

The aromatic diamine 4-aminopirydine was used for the synthesis of a series of supramolecular metal-organic sulfate salts. The obtained compounds with the formula $(C_5H_7N_2)_2[M^{II}(H_2O)_6](SO_4)_2$ (M^{II}= Fe, Co, Ni, Cu and Zn) and $(C_5H_7N_2)_2[Mn(H_2O)_4(SO_4)_2]$ crystallize with a triclinic symmetry (S.G. $P\bar{1}$). These complexes possess a hybrid structure type with an interlayer distance that varies from 10 to 12 Å depending on the metal. The fact that the crystal structure is supramolecular, the mineral layer is built from hydrogen bonds only and the interlayer space is filled with aromatic diamines that form chains through π…π interactions. The thermal study *in-situ* of all metal compounds revealed an important stability with the formation of crystalline phases during heating. The dehydration proceeds differently according to the metal incorporated into the structure.

Keywords: Sulfate salts, Thermal decomposition, Hybrid layered materials, Crystal structure, transition metals.

1. Introduction

Organic-inorganic hybrid materials constitute a large and diverse class of materials thanks to the improvement of their chemistry through which it was possible to gather both organic and inorganic components and benefit properties from the different parts [1-5]. Hybrid layered materials, through their two dimensional structures that consist in stacked inorganic sheets with intercalated organic guests, have great importance in different fields of applications, such as nonlinear optical materials, conductors, photoactive materials, nanomagnets, polymer additives and ion-exchangers [6-8]. Various types of hybrid porous coordination polymers [9] and 2D metal organic frameworks [10] exhibit selective catalytic activities towards many small organic molecules. Layered structures governed by weak bonding energy in one or two lattice directions make them very useful in intercalation and desintercalation processes in the field of adsorption, ionic and electronic conduction and the catalytic reactions [11-13]. Their thermal stability gives them an interesting property to cover other potential applications [14,15]. The particular use of an amine in different types of hybrid complexes as an organic part was developed. The important role of the protonated amine as a ‘‘template’’ [16,18] and its usefulness in many application areas such as optics and catalysis [19,21] was described. In almost all these materials, organic cations interact with the mineral part through hydrogen bonding. On the other hand, the supramolecular hybrid materials represent also an interesting opportunity for the development of new materials in different applications, as dielectrics, semiconductors or NLO materials [22,23]. Among them, many sulfates and selenates have been elaborated using organic molecules as templates, while cations involved in their syntheses have included transition metals [24-31], lanthanides [32] and actinides [33]. The diversity of structure framework dimensionality that could be built from chains, layers, or three dimensional connections was mentioned. Among other, more results are uncovered for potential applications as regards amine metal sulfate with zero-dimensional

structure belonging to alums and Tutton's salts [34,36]. In this context, we are interested in mixed transition metal sulfates and protonated amines. We demonstrated through previous work, that the use of an aromatic diamine or monoamine template in the synthesis of hybrid double sulfate salts containing transition metals provided a new structure topology, that gathers the supramolecular and the lamellar aspect [37,39]. Despite the supramolecular network constructed by weak hydrogen bonds and interactions, an important thermal stability similar to that of lamellar materials has been demonstrated. Previously, hybrid lamellar M(II)-sulfate compounds have been developed by our group for their pertinent properties such as magnetic, magneto-electronic and catalytic properties [40-43]. We have also demonstrate the anti-microbial, anti-fungal and antioxidant activities of the $(C_6H_9N_2)_2[M^{II}(H_2O)_6](SO4)_2{\cdot}2H_2O$ with M = Co and Ni [44]. In the continuity of our activity and to more investigate the influence of aromaticity in these types of materials we introduce like organic part the amine 4-aminopyridine ($C_5H_6N_2$). This later is a diamine very soluble in water and its conformation presents a heterocycle with carbon atom in the "para" position of the aromatic N linked to $-NH_2$ group. Recently, Pietraszko and al. [45] reported a series of twelve new metal sulfates templated by 4-aminopyridine, with the following compositions: $(C_5H_7N_2)_2[M^{II}(H_2O)_6](SO_4)_2$ (M^{II} = Cu, Co, Mg, Zn, Fe, Mn), $(C_5H_7N_2)_2[M^{II}(H_2O)_4(SO_4)]{\cdot}4H_2O$ (M^{II} = Mn, Cd), $(C_5H_7N_2)_2[Cd(H_2O)_4(SO_4)]$, $(C_5H_7N_2)_2[Mn(H_2O)_4(SO_4)]$, $(C_5H_7N_2)_2[M^{II}(H_2O)_4(SO_4)]{\cdot}4H_2O$ and $(C_5H_7N_2)_2[Fe^{III}(H_2O)_4(SO_4)]$, without showing their important thermal behavior related to the lamellar structure characters. For these reasons, a family of hybrid sulfates with general formulas $(C_5H_7N_2)_2[M^{II}(H_2O)_6](SO_4)_2$ with (M^{II}= Zn, Cu, Ni, Co and Fe) and $(C_5H_7N_2)_2[Mn(SO_4)_2(H_2O)_4]$ was prepared. A short structure description was given by detailing the lamellar and supramolecular morphology and the systematic study of the thermal behavior of all materials *in situ* was performed.

2. Experimental

2.1. Materials

$MnSO_4 \cdot H_2O$ (Prolabo), $FeSO_4 \cdot 7H_2O$ (Merck), $CoSO_4 \cdot 6H_2O$ (Prolabo), $NiSO_4 \cdot 6H_2O$ (Aldrich Chemie), $CuSO_4 \cdot 5H_2O$ (Acros Organics), $ZnSO_4 \cdot 7H_2O$ (Carlo, Erba), 4-aminopyridine ($C_5H_7N_2$) (Sigma Aldrich), and H_2SO_4 (Aldrich).

2.2 Synthesis

Crystals of materials with the general formulas $(C_5H_7N_2)_2[M^{II}(H_2O)_6](SO_4)_2$ with (M^{II} = Fe, Co, Ni, Cu and Zn) and $(C_5H_7N_2)_2[Mn(H_2O)_4(SO_4)_2]$ were obtained by crystallization in solution at room temperature (slow evaporation method). The metal sulfate hydrates $M^{II}SO_4.nH_2O$ and 4-aminopyridine (PRD) were dissolved in 10 ml of distilled water by magnetic stirring, which was acidified by dropwise addition of concentrated sulfuric acid H_2SO_4 ($2 \leq pH \leq 3$) until the solution becomes clear. The molar ratio of 1 metal/2 amines is used in the preparation of each **M^{II} PRD** solution (M^{II} = Co, Ni, Cu and Ni), whereas the proportions 1 metal /3 amine were exploited for the synthesis of compounds based on Fe and Mn. The formed crystals were collected by filtration and washed with a small amount of distilled water before being dried in ambient air.

2.3. Single-Crystal X-ray Diffraction

A suitable crystal of each compound was glued to a glass fiber mounted on APEX II area detector 4-circles diffractometer. Intensity data sets were collected using Mo-Kα radiation (0.71073 A) through the Bruker AXS APEX2 Software Suite. The crystal structure of compounds possessing the general formulas $(C_5H_7N_2)_2[M^{II}(H_2O)_6](SO_4)_2$ with (M^{II} = Fe, Co, Ni, Cu and Zn) and $(C_5H_7N_2)_2[Mn(SO_4)_2(H_2O)_4]$ was determined in the triclinic symmetry, space group $P\bar{1}$. The atoms of the metal, sulfur, oxygen and the nitrogen of the aromatic amine were located using the

direct methods with the program SIR97 [46]. The positions of the carbon atoms of amine molecule were found from successive difference Fourier calculations using SHELXL97 [47]. The hydrogen atoms linked to the carbons were fixed geometrically and restrained via HFIX command of SHELXL97 program, while the other hydrogen atoms were found and refined by several cycles of refinements. Within a water molecule, the O–H and H–H distances have been restrained to give the ideal value for H–O–H angle. The atomic displacement parameters of the H atoms were fixed at 1.5 U_{eq} of their parent atom.

2.4. Thermal analysis measurements

Variable temperature powder X-Ray diffraction (VT-PXRD) analysis was carried out using a θ–θ Bruker AXS D8 Advance powder diffractometer, equipped with a high-temperature Anton Paar HTK1200 oven camera and a LynxEye detector. Powder patterns were collected sequentially upon heating at 21.6 1°C.h^{-1} up to 400.1°C, with the monochromatized CuKα1 radiation (λ=1.5406 Å). To ensure satisfactory counting statistics, counting times of 20 min/pattern were selected for the thermal decomposition of the precursors, so that any pattern could be collected within a temperature range of 7.2°C. TGA–DSC measurements were performed using a TA SDT Q600 instrument in flowing air, for any compound, with a heating rate of 0.5 °C min^{-1} up to 600 °C.

3. Results and discussion

3.1. Supramolecular and lamellar aspects of the crystal structures

All compounds with general formula $(C_5H_7N_2)_2[M^{II}(H_2O)_6](SO_4)_2$ (M^{II} = Fe, Co, Ni, Cu and Zn) are isostructural and crystallize in the triclinic system, with the space group $P\bar{1}$. The complex $(C_5H_7N_2)_2[Mn(H_2O)_4(SO_4)_2]$ crystallizes in the $P\bar{1}$ space group also, but with a *c* parameter, and cell volume smaller than those observed in $(C_5H_7N_2)_2[M^{II}(H_2O)_6](SO_4)_2$ [45]. The crystal

structure (*pseudo 2D*) is supramolecular with a lamellar character. It is constructed by a lamellar stack of anionic inorganic layers parallel to the (a, c) plane, between which are incorporated the organic cations 4-aminopyridinium $(C_5H_7N_2)^+$ to compensate the negative charge brought by the mineral part. The development of an inorganic layer is based on the association of mineral units, *i.e.* sulfates $(SO_4)^{2-}$ and metal octahedral $[M^{II}(H_2O)_6]^{2+}$ **(Fig. 1)**, or trimeric units $[Mn(H_2O)_4(SO_4)_2]^{2-}$ **(Fig. 2)**, which are formed by metal octahedra that share two vertices with two sulfate tetrahedra. Inorganic entities are stabilized and interconnected by hydrogen bonds only. This leads to the formation of a *pseudo* two-dimensional mineral layer parallel to the (a, b) plane. By reason of the steric hindrance of the organic part and the shape of the mineral layer, the distance between the median planes of two adjacent inorganic layers may vary from 10 Å to 12 Å. In fact, it corresponds to the value of the c parameter of the crystal cell **(Fig. 3)**. The comparative study between the interlamellar distances of all compounds shows the Jean Teller effect, which appear in the copper compound, that decrease this distance, whereas the smallest interlayer distance was observed in the manganese based material due to the trimeric units of the mineral parts **(Table 1)**.

It must be note that the amine template incorporated into the structure plays an important role to change the interlamellar distance. Indeed, the organic–inorganic sulfate salts incorporating α-methylbenzylamine $(C_8H_{12}N)_2[M^{II}(H_2O)_4(SO_4)_2]\cdot 2H_2O$ (M = Fe to Zn) where the layers are built from mineral entities exhibiting more important interlamellar distance i.e. 16 Å [37] whereas the material $La_2(H_2O)_2(C_4H_{12}N_2)(SO_4)_4$ used piperazine molecule for the organic part possesses an interlamellar distance equals to 13.4 Å [48]. On the other hand, the interlamellar distances can be changed according to the orientation of the incorpored amine between the inorganic layers. In fact, the perpendicular orientation of benzimidazole in the structure type of

$(C_7H_7N_2)_2[M^{II}(H_2O)_6](SO_4)_2.4H_2O$ possesses an interlayer distance equals to 13,29 Å which decreasing to 12.33 Å in the horizental orientation [39]. The most important interlamellar distances are observed in 2D structures containing condensed sheets formed by covalent or ionocovalent bonds as greater distances can be observed [49,50]. The cohesion of the crystal structure in the three dimensions is ensured by hydrogen bonds type OW-H···O between the inorganic entities and N-H···O connecting the mineral part and the organic part and π···π interactions between the aromatic rings of the protonated amines. However, the aromatic interactions *via* the amines rings are made according parallel-displaced configuration [51,52]. The cohesion of the structure provided by hydrogen bonds and weak interactions confers to the material an important stability. Indeed, the coulomb attraction generated firstly between organic and inorganic parts, assured by the charge-assisted N– H·····$O^{(-)}$ hydrogen bond, which plays role to organist the adjacent layers. On other hand the O–H·····$O^{(-)}$ charge assisted intermolecular hydrogen bond, created between the water molecule and the sulfate group, is considered as the driving force of the inorganic layer formation. This type of strong hydrogen bonding especially between the organic part and the inorganic framework promotes the stability of the crystal structure [53-60]. Despite the consideration of the supramolecular aspect of the inorganic layer, these compounds define an unusual lamellar topology with a fully supramolecular network in the family of sulfates and their derivatives.

3.2. Thermal decomposition

Crystallographic study has identified a fully supramolecular structural network which generating a lamellar appearance. Nevertheless, the simultaneous presence of lamellar and supramolecular features in the structure of our precursors justifies the need to investigate if this new lamellar behavior, built only from weak bonds and interactions, can provide a useful property related to

this well-known structure type in many compounds such as clays that have a lamellar structures, but constructed by strong covalent bonds. It is known that lamellar materials like clay minerals or montmorillonite [61] and some hybrid layered materials as many phosphonates, used for intercalation and catalytic reactions [62-63] have an important thermal stability. Indeed, they can operate at moderate temperature, for environmentally friendly processes to produce fine chemicals [64-65] or for adsorption and ion-exchange [66]. In this context, we are interested in performing a thorough thermal study to investigate thermal stability of our precursors. According to previous works, the thermal decomposition of these types of compounds may be influenced by the nature of the transition metal incorporated in their isotypical crystal structures [67,68] The thermal behavior study of the synthesized materials is made *in situ* by X-ray diffraction (VT-PXRD) and thermogravimetry (TG). Generally, the thermogravimetric analysis shows that for all the precursors the thermal dehydration occurs in the first place, and the obtained anhydrous phase exists over a wide range of temperature (Important bearing on the TG curve). Then, the decomposition leads to final residue which may be metal sulfate, or metal oxide, or a mixture of metal sulfate and metal oxide. The structural evolution of precursors $(C_5H_7N_2)_2[M^{II}(H_2O)_6](SO_4)_2$ with (M^{II} = Cu, Ni, Zn, Co and Fe) and $(C_5H_7N_2)_2[Mn(H_2O)_4(SO_4)_2]$ depend on the metal, and transformations differ in temperature ranges and crystallinity of phases. All dehydration steps of synthesized compounds begin with the weight loss of 0.5 H_2O.

3.2.1. Thermal dehydration of $(C_5H_7N_2)_2[Zn(H_2O)_6](SO_4)_2$

The thermogravimetric analysis carried out on $(C_5H_7N_2)_2[Zn(H_2O)_6](SO_4)_2$ **(Fig. 4)** shows that this material undergoes a complete dehydration between room temperature and 70°C accompanied by endothermic DSC signal towards 55°C. The departure of six coordinated water

molecules, which corresponds to an experimental weight loss of 19.57% (theoretical value 19.42%), occurs in two steps. In this temperature range, we observe on the TG curve a small landing at 30 °C indicating a first mass loss of 0.5 H_2O (experimental value 1.17%, theoretical value 1.61%). Then a second loss, most important, of 5.5 H_2O remaining (mass loss observed 18.40%, theoretical mass loss 17.80%) giving rise to a significant second bearing which defines a whole domain of stability of the resulting anhydrous compound $(C_5H_7N_2)_2Zn(SO_4)_2$ between 70 and 220 °C. From this temperature, the anhydrous phase decomposes to give the final residue ZnO at 600 °C. The TG curve shows that the decomposition takes place according to a successive masse losses characterized by two endothermic peaks between 270 and 400 °C and one exothermic peak between 500 and 600 °C. The powder diffraction data according to the temperature **(Fig. 5)** indicates a sudden structural transition at 56 °C which is due, most probably, to the departure of 0.5 H_2O. The compound obtained with 5.5 H_2O is crystallized and remains stable until about 114 °C. The anhydrous phase $(C_5H_7N_2)_2Zn(SO_4)_2$ formed after, undergone a structural change at 185 °C and its decomposition starts at 235 °C giving rise to crystalline phases in the first place, then to amorphous phases.

3.2.2. Thermal dehydration of $(C_5H_7N_2)_2[Ni(H_2O)_6](SO_4)_2$

The thermogravimetric analysis of the crude synthetic compound $(C_5H_7N_2)_2[Ni(H_2O)_6](SO_4)_2$ **(Fig. 6)** shows a weight loss of 21.49% beginning at room temperature and ending at 100 °C, which is in agreement with the departure of six water molecules per formula unit (theoretical loss 19.59%). The departure of the totality of water molecules is done in three steps. Previously, It happens a small weight loss of 2.02% (Theoretical value 1.63%) corresponding to the departure of 0.5 H_2O leading to the formation of an intermediate phase with the formula $(C_5H_7N_2)_2[Ni(H_2O)_{5.5}](SO_4)_2$ at about 30 °C. Then, another hydrated intermediate

$(C_5H_7N_2)_2[Ni(H_2O)_3](SO_4)_2$ which is not stable (no bearing on the TG curve) is formed at 100 °C after the weight loss of 3 water molecule (experimental value 9.48%, theoretical value 9.79%). The departure of the remaining quantity of water occurs between 100 °C and 130 °C. The three thermodifferential signals associated to the dehydration are endothermic and with low intensity. The anhydrous compound $(C_5H_7N_2)_2Ni(SO_4)_2$ thus formed crystallizes from 135 ° C and remains stable up to 190 °C. Beyond this temperature the decomposition of the anhydrous phase, coupled by an exothermic pic, proceeds leading to the obtaining of the final product 0.5 ($NiO + NiSO_4$) between 500 °C and 600 °C which is the final residue of 19.14% (theoretical value, 20.83%). The thermal study by powder diffraction of $(C_5H_7N_2)_2[Ni(H_2O)_6](SO_4)_2$ **(Fig. 7)** indicates that the departure of 0.5 H_2O at 58 °C causes a small change in the diffraction patterns which is due to the disappearance of some lines, contrary to sudden and significant change observed in the Zn, Fe and Cu-based compounds. At 108 °C, the hydrated phase $(C_5H_7N_2)_2[Ni(H_2O)_3](SO_4)_2$ is formed. According to VT-PXRD, it seems to be with low crystallinity or almost amorphous up to 137 °C. Beyond this temperature the anhydrous phase crystallizes and remains stable between 137 °C and 194 °C. During the decomposition of $(C_5H_7N_2)_2Ni(SO_4)_2$, which starts at 194 °C, the diffraction lines show the presence of a crystalline phase which is stable up to 400 °C.

3.2.3. Thermal dehydration of $(C_5H_7N_2)_2[Cu(H_2O)_6](SO_4)_2$

Starting from CuPRD formula deduced from the structural study, *i.e.* $(C_5H_7N_2)_2[Cu(H_2O)_6](SO_4)_2$ the thermogravimetric analysis carried out on this compound **(Fig. 8)** shows that it undergoes a complete dehydration accompanied by endothermic DSC peaks and loses six molecules of water between room temperature and 150 °C (experimental weight loss 22.47 %, theoretical mass loss 19.42 %). Firstly it occurs an immediate loss of mass of 0.5 H_2O

at 35 °C leading to the formation of $(C_5H_7N_2)_2[Cu(H_2O)_{5.5}](SO_4)_2$ (experimental value 1.11%, theoretical value 1.61%), then a larger mass loss of about 17.92% corresponding to the departure of 5 H_2O at about 90 °C (theoretical value 16.18%) giving rise to the hydrated phase $(C_5H_7N_2)_2[Cu(H_2O)](SO_4)_2$. After, the plot shows a bearing and no significant loss of mass is recorded up to 190 °C. Indeed, the formed anhydrous phase $(C_5H_7N_2)_2Cu(SO_4)_2$ is stable over this temperature range. Beyond this, the decomposition of the anhydrous phase proceeds and probably leads to the formation of copper sulfate $CuSO_4$ between 420 and 550 °C. The thermodiffractometry of $(C_5H_7N_2)_2[Cu(H_2O)_6](SO_4)_2$ **(Fig. 9)** indicates a sudden structural transition at 56 °C which is due most probably to the departure of 0.5 H_2O. The compound obtained with 5.5 H_2O is crystallized and remains stable until about 100 °C. Between this temperature and 190 °C, the diffraction lines show the coexistence of two crystalline phases, it is probably the formation of the anhydrous phase $(C_5H_7N_2)_2Cu(SO_4)_2$ with the other monohydrated phase $(C_5H_7N_2)_2[Cu(H_2O)](SO_4)_2$. After 190 °C, the anhydrous product remains stable up to 314 °C. Copper sulfate $CuSO_4$ (PDF Number: 00-014-0373) begins to appear from 271 °C and continues to manifest for higher temperatures.

3.2.4. Thermal dehydration of $(C_5H_7N_2)_2[Co(H_2O)_6](SO_4)_2$ and $(C_5H_7N_2)_2[Fe(H_2O)_6](SO_4)_2$

The thermal behavior of the cobalt-based material **(Fig. 10)** is similar to the iron-based **(Fig. 11)**. The thermogravimetric analysis carried out on $(C_5H_7N_2)_2[Co(H_2O)_6](SO_4)_2$ shows that it undergoes complete dehydration and loses six molecules of water between room temperature and 120 °C (experimental weight loss 21.49%, theoretical mass loss 19.58%). A Rapid loss of weight of 1.71%, observed on the TG curve at 30 °C and accompanied with a little endothermic DSC peak, is attributed to the departure of 0.5 molecule of water (calculated mass loss, 1.63%) to

obtain $(C_5H_7N_2)_2[Co(H_2O)_{5.5}](SO_4)_2$. A second mass loss corresponding to the departure of the remaining 5.5 molecules of water and providing an endothermic DSC peak is observed on the TG curve between 50 and 120 °C. The formation of the anhydrous phase $(C_5H_7N_2)_2Co(SO_4)_2$ takes place after, up to the begin of the decomposition stage at about 220 °C. This decomposition, accompanied by an exothermic DSC peak, ends by the formation of the cobalt sulfate $CoSO_4$ as final residue between 480°C and 600 °C (experimental value 27.75%, theoretical value 28.10%). At this stage, the decomposition of the anhydrous phase of the iron based compound, i.e. $(C_5H_7N_2)_2Fe(SO_4)_2$, led to the formation, at first time, of iron sulfate $FeSO_4$ at 450 °C (experimental percentage of residue 26.6%, theoretical percentage of residue 27.68%) and to the formation of iron oxide FeO at 600 °C, in a second time, as final residue (experimental percentage 14.93%, theoretical percentage 13.1%). The phase changes reported from X-ray powder diffraction study according to the temperature of $(C_5H_7N_2)_2[Fe(H_2O)_6](SO_4)_2$ **(Fig .12)** are in agreement with the mass loss observed in the TG curve of CoPRD **(Fig .13)**. Indeed, the departure of 0.5 H_2O causes a small change in the shape of the diffraction patterns at 71 °C. Thus, the crystallized phase $(C_5H_7N_2)_2[Fe(H_2O)_{5.5}](SO_4)_2$ appears and remains stable up to 113 °C. After full dehydration, the anhydrous phase $(C_5H_7N_2)_2Fe(SO_4)_2$ occurs with low cristallinity and remains stable between 113 and 232 °C. From this temperature, it begins to decompose with a change in the shape of the diffraction patterns indicating the formation of crystallized phases at higher temperatures.

3.2.5. Thermal dehydration of $(C_5H_7N_2)_2[Mn(H_2O)_4](SO_4)_2$

Thermogravimetric analysis **(Fig.14)** and thermo diffraction **(Fig.15)** of $(C_5H_7N_2)_2[Mn(H_2O)_4](SO_4)_2$ allow to study its thermal behavior. The TG curve shows that the dehydration of the precursor corresponding to the departure of the four coordinating water molecules is done in two stages from room temperature to 100 °C. The first mass loss of 1.36%

(theoretical value 1.76%) corresponding to the departure of 0.5 H_2O, gives rise to the intermediate hydrate $(C_5H_7N_2)_2[Mn(H_2O)_{3.5}](SO_4)_2$ at 40 °C. The second loss of 12.71% (calculated loss 12.37%) leading to the formation of the anhydrous $(C_5H_7N_2)_2Mn(SO_4)_2$ corresponds to the departure of 3.5 H_2O. The two steps of dehydration are accompanied by two endothermic peaks as shown in the DSC signal trace. Between 100 and 200 °C, the thermogravimetric curve shows a plateau indicating the stability domain of the formed anhydrous phase. At 200 °C, the product starts to decompose to give manganese sulfate $MnSO_4$ as final residue at 450 °C (experimental value 29.19%, theoretical value29.66%). In the decomposition of the anhydrous phase, the two first mass losses of the order of 14.88% and 9.12% are characterized by two endothermic peaks on the DSC curve. The exothermic peak observed at 420 °C indicates the crystallization of manganese sulfate. The *in situ* study by X-ray diffraction **(Fig.15)** shows a small change in the shape of diffraction patterns at 71 °C which is due to the departure of 0.5 H_2O and another remarkable change indicating the formation of the anhydrous phase $(C_5H_7N_2)_2Mn(SO_4)_2$, which crystallizes at 99 °C. According to the **(Fig.15)**, this phase undergoes decomposition at 246 °C.

4. Effect of the dehydration on the crystal structures

To study the effect of the partial dehydration of $(C_5H_7N_2)_2[Zn(H_2O)_6](SO_4)_2$ and $(C_5H_7N_2)_2[Co(H_2O)_6](SO_4)_2$ on the structures, their powder X-Ray diffraction spectra were recorded at different temperature around their first dehydration temperature (30 °C), and the obtained spectra are presented in the supplementary file (figures S1 and S2). The collected results demonstrate that the departure of 0.5 H_2O does not affected the crystallinity of the partial dehydrated compounds. In fact, this first stage of dehydration to an amount of $5.5H_2O$ involves subtle changes in the powder diffraction patterns, such as small peak displacement for

$(C_5H_7N_2)_2[Zn(H_2O)_6](SO_4)_2$ or slight modifications in diffraction line intensities in $(C_5H_7N_2)_2[Co(H_2O)_6](SO_4)_2$ for example.

To insight more within the structure of the dehydrated compounds, a pattern of $(C_5H_7N_2)_2Fe(SO_4)_2$ collected at 110 °C could be indexed with the program DICVOL06 [69] on the basis of the first 20 available diffraction lines, leading the triclinic unit cell a = 6.677(2) Å, b = 7.474(2) Å, c = 10.407(4) Å, α = 82.13(3)°, β= 83.89(3)°, γ = 74.24(3)°, V = 493.8 Å3 [M_{20} = 40; F_{20} = 81(0.007;36)]. Regarding the unit cell of the hexa-hydrated precursor, it is clear that the departure of the water molecules involves decreasing the interlayer space from 12.5 Å to 10.4 Å, while the cell volume decrases of about 5%. The a and c cell parameters are moderately modified, due to the re-organization of the sulfate groups around Fe atoms, free of water molecules. It is obvious here that the lamellar character is preserved upon dehydration. This decrease of the interlayer distance results from the condensation of the inorganic network and the metal is probably hexa-coordinated to the six oxygen atoms of the sulfate groups. Hence, the dehydration of the compound leads to the stabilization of Fe-sulfate layers. Then the metal keeps its Lewis acidity and no influence on the dehydration process is observed.

Conclusion

As demonstrated above, the association of organic and inorganic parts gives rise to a lamellar topology of crystal structure with a fully supramolecular network. In addition, the interlamellar distance registered by all compounds varied from 10 Å to 12 Å depend on the nature of transition metal and can modified by the Jean teller effect. It must be note that the stability of the crystal structure in three dimensions assured by hydrogen bonds O-H···O between the inorganic entities and N-H···O linked the mineral part to the organic part and π···π interactions between the

aromatic rings of protonated amines. The study of the thermal decomposition of all materials shows that the dehydration stage gives several successive crystalline phases and the anhydrous compound thus formed is thermally stable over a significant range of temperature. Despite their dehydration, these structures keep their good crystallinity as well as their lamellar form and the decrease of the interlayer distance is confirmed. In the future, it would be interesting to test our synthesized precursors for possible catalytic reactions and the results reported here give confidence in the possibility of preparing new sulfate-based materials in the presence of amines with varied structure topologies.

Conflict of Interest

The authors declare that they have no conflict of interest.

Notes and references

Crystallographic data for complexes **1** and **2** are available from the Cambridge Crystallographic Data Centre, with CCDC No. 1039275, for polymorph **1**, and No. 1039276 for polymorph **2**. Copies of these data can be obtained free of charge from the Cambridge Crystallographic Data Centre, 12 Union Road, Cambridge CB2 1EZ, UK; fax: (+44) 1223-336-033; or e-mail: deposit@ccdc.cam.ac.uk.

References

[1] C. Sanchez, B. Julian, P. Belleville, M. Popall, J. Mater. Chem. **15**, 3559 (2005).

[2] A. L. Mohana Reddy, S. R. Gowda, M. M. Shaijumon and P. M. Ajayan, Adv. Mater. **24**, 5045, (2012).

[3] C. Sanchez and P. Belleville, Chem. Soc. Rev. **40**, 696, (2011).

[4] A. Dolbecq, E. Dumas, C. R. Mayer and P. Mialane, Chem. Rev. **110**, 6009, (2010).

[5] C. N. R.Rao, A. K. Cheetham and A. J. Thirumurugan, Phys. Condens. Matter. **20**, 083202, (2008).

[6] C. Sanchez, G.J. de A.A. Soler-Illia, F. Ribot, T. Lalot, C.R. Mayer, V. Cabuil, Chem. Mater. **13, 10**, 3061, (2001).

[7] A. L. Mohana Reddy, S. R. Gowda, M. M. Shaijumon and P. M. Ajayan, Adv. Mater. **24**, 5045, (2012).

[8] G.F. Swiegers, T.J. Malefetse, Coord. Chem. Rev. 225, 91 (2002).

[9] M. Higuchi, D. Tanaka, S. Horike, H. Sakamoto, K. Nakamura, Y. Takashima, Y. Hijikata, N. Yanai, J.Kim, K. Kato, Y. Kubota, M. Takata and S. Kitagawa, J. Am. Chem. Soc. **131**, 10336, (2009).

[10] J. Lee, O. K. Farha, J. Roberts, K. A. Scheidt, S. T. Nguyen and J. T. Hupp, Chem. Soc. Rev. **38**, 1450, (2009).

[11] G. Centi and S. Perathoner, Microporous Mesoporous Mater. **107**, 3, (2008).

[12] K. H. Goh, T. T. Lim and Z. Dong, Water Res. **42**, 1343, (2008).

[13] S. Z. Butler, S. M. Hollen, L. Cao, Y. Cui, J. A. Gupta, H. R. Gutie, T. F. Heinz, S. S. Hong, J. Huang, A. F. Ismach, E. Johnstonhalperin, M. Kuno, V. V. Plashnitsa, R. D. Robinson, R. S. Ruoff, S. Salahuddin, J. Shan, L. Shi, O. M. G. Spencer, M. Terrones, W. Windl and J. E. Goldberger, ACS Nano, **7**, 2898, 2(013).

[14] W. Xie, R. Xie, W. Pan, D. Hunter, B. Koene, L. Tan and R. Vaia, Chem. Mater., **14**, 4837, (2002).

[15] T. W. Kim, H. W. Ha, M. J. Paek, S. H. Hyun, I. H. Baek, J. H. Choy and S. J. Hwang, J. Phys. Chem. C. **112**, 14853, (2008).

[16] C. Ge´ rardin, T. Loiseau, G. Fe´ rey, F. Taulelle and A. Navrotsky, Chem. Mater.**14**, 3181, (2002).

[17] H. B. Yao, M. R. Gao and S. H. Yu, Nanoscale, **2**, 323, (2010).

[18] C. N. R. Rao, S. Natarajan, A. Choudhury, S. Neeraj and A. A. Ayi, Acc. Chem. Res. **34, 80**, (2001).

[19] N. Leblanc, M. Allain, N. Mercier and L. Sanguinet, Cryst. Growth Des. **11**, 2064, (2011).

[20] W. Bi, N. Louvain, N. Mercier, J. Luc, I. Rau, F. Kajzar and B. Sahraoui, Adv. Mater. **20**, 1013, (2008).

[21] P. Wight and M. E. Davis, Chem. Rev. **102**, 3589, (2002).

[22] R. Masse and J. Zyss, European Patent EP 0 488 869 B1 (1996).

[23] N. Leblanc, N. Mercier, L. Zorina, S. Simonov, P. Auban-Senzier and C. Pasquier,JACS **133**,14924, (2011).

[24] C. N. R. Rao, J. N. Behera and M. Dan, Chem. Soc. Rev. **35**, 375, (2006).

[25] H. Naïli, M. François, A. J. Norquist, W. Rekik, Solid State Sci. **74**, 44, (2017).

[26] N. L. Nkhili, W. Rekik, T. Mhiri, K.T. Mahmudov, M. N. Kopylovich and H. Naïli, Inorganica Chim. Acta. **412**, 27, (2014).

[27] N.L. Nkhili, W. Rekik, H. Naïli, T. Mhiri, T. Bataille, Arab. J. Chem. **10**, S2509, (2017).

[28] W. Rekik, H. Naïli a, T. Mhiri, T. Bataille, Solid State Sci. **14**, 1503, (2012).

[29] S. Yahyaoui, W. Rekik, H. Naïli, T. Mhiri, T. Bataille, J. Solid State Chem. **180,** 3560, (2007).

[30] F. Hajlaoui, S. Yahyaoui, H. Naïli, T. Mhiri, T. Bataille, Polyhedron. **28**, 2113, (2009).

[31] F. Hajlaoui, S. Yahyaoui, Houcine Naïli, T. Mhiri, T. Bataille, Inorganica Chim. Acta. **363**, 691 (2010)

[32] T. Bataille and D. ̈Louer, J. Solid State Chem. **177**, 1235, (2004).

[33] A. J. Norquist, M. B. Doran and D. O'Hare, Inorg. Chem. **44**, 3837, (2005).

[34] M. Fleck, L. Bohaty and E.́ Tillmanns, Solid State Sci. **6**, 469, (2004).

[35] T. Bataille, Acta Crystallogr., Sect. C: Cryst. Struct. Commun. **59**, 459, (2003).

[36] W. Rekik, H. Naïli, T. Mhiri and T. Bataille, Acta Crystallogr., Sect. E: Struct. Rep. **61**, 629, (2005).

[37] O. Kammoun, T. Bataille, A. Lucas, V. Dorcet, I. Marlart, W. Rekik, H. Naıli, and T. Mhiri, Inorg. Chem. **53**, 2619, (2014).

[38] O. Kammoun, W. Rekik, H. Naïli, and T. Bataille, J. Org. Chem. **136**, 741, (2013).

[39] O. Kammoun , W. Rekik, H. Naïli and T. Bataille, New. J. Chem. **39**, 2682, (2015).

[40] W. Rekik, H. Naïli, T. Mhiri and T. Bataille, Mater. Res. Bull. **43**, 2709, (2008).

[41] O. Kammoun, H. Naïli, W. Rekik and T. Bataille, Inorganica Chim. Acta. **434**, 209, (2015).

[42] N. Hfidhi, M. Korb, M. Fitta, E. Čižmár, H. Lang and H. Naïli, *Inorganica Chim. Acta*. **484**, 206, (2019)

[43] O. Kammoun, W. Rekik, T. Bataille, K. T. Mahmudov, M. N. Kopylovich and H. Naïli, J. Org. Chem. **741-742**, 136, (2013).

[44] S. Saïd, R. Ben Abdallah Kolsi and H. Naïli J. Organomet. Chem. **809**, 45, (2016).

[45] T.J. Bednarchuk, V.Kinzhybalo, O. Bednarchuk, A.Pietraszko, J. Mol. Struct. **1120**, 138, (2016).

[46] A. Altomare, M.C. Burla, M. Camalli, G.L. Cascarano, C. Giacovazzo, A. Guagliardi, A. G. G. Moliterni, G. Polidori and R. Spagna, J. Appl. Crystallogr, **32**, 115, (1999).

[47] G.M. Sheldrick, Acta Crystallogr. Sect. A. **64**, 112, (2008).

[48] T. Bataille and D. Louer, J. Mater. Chem. **12**, 3487, 2002.

[49] F. Leroux, C. Taviot-Gueho, J. Mater. Chem. **15**, 3628, (2005).

[50] T. Nakamura, M. Ogawa, Langmuir, **28**, 7505, (2012).

[51] C. Janiak, J. Chem. Soc., Dalton Trans. 3885, (2000).

[52] N. Jiten Singh, S. K. Min, D. Y. Kim and K. S. Kim, J. Chem.Theory Comput. **5**, 515, (2009).

[53] D. Mekhatria, S. Rigolet, C. Janiak and A. Simon-Masseron, Cryst. Growth Des. **11**, 396, (2011).

[54] B.G. Hernandez, J.K. Maclaren, H.A. Hoppe, J. Pasan, J. Sanchiz, C. Janiak, CrystEngComm. **14**, 2635, (2012).

[55] J. K. Maclaren and C. Janiak, Inorg. Chim. Acta, **389**, 183, (2012).

[56] A.C. Chamayoua, M.A. Neelakantan, S. Thalamuthu and C. Janiak, Inorg. Chim. Acta, **365**, 447, (2011).

[57] B.G. Hernandez, H.A. Hoppe, J.K. Vieth, J. Sanchiz and C. Janiak, Chem. Com. **46**, 8270, (2010).

[58] B.M. Draskovi, G.A. Bogdanovic, M.A. Neelakantan, A.C. Chamayou, S. Thalamuthu, Y.S. Avadhut, J.S. Gunne, S. Banerjee and C. Janiak, Cryst. Growth Des, **10**, 1665, (2010).

[59] B. Wu, X. Huang, Y. Xia, X.J. Yang, C. Janiak, CrystEngComm. **9**, 676, (2007).

[60] T. Dorn, C. Janiak, K.A. Shandi, CrystEngComm. 7, 633, (2005).

[61] Y. Zidane, A. Ourari, T. Bataille, P. Hapiot, D. Hauchard, J. Electroanal. Chem. **641**, 64, (2010).

[62] G. Alberti, M. Casciola, U. Costantino, R. Vivani, Adv. Mater. **8**, 291, (1996).

[63] K. D. Demadis, N. Famelis, A. Cabeza, M.A.G. Aranda, R.M.P. Colodredo, A. I. Molina, Inorg.Chem. **51**, 7889, (2012).

[64] I. Rodriguez, M. Climent, S. Iborra, V. Fornes and A. Corma, J. Catal. **192**, 441, (2000).

[65] C. Tagusagawa, A. Takagaki, S. Hayashi and K. Domen, J. Am. Chem. Soc. **130**, 7230, (2008).

[66] A. I. Khan, A. Ragavan, B. Fong, C. Markland, M. O'Brien, T. G. Dunbar, G. R. Williams and D. O'Hare, Ind. Eng. Chem. Res. **48**, 10196, (2009).

[67] Nelwamondo, A. N.; Eve, D. J.; Watkins, G. M.; Brown, M. E. Thermochim. Acta. **318**, 165, (1998).

[68] Yuvaraj, S.; Fan-Yuan, L.; Tsong-Huei, C.; Chuin-Tih, Y. J. Phys. Chem. **107**, 1044, (2003).

[69] A. Boultif and D. Louër, J. Appl. Crystallogr. **5**, 724, (2004).

Figure captions

Fig. 1: Supramolecular aspect of the inorganic layer of $(C_5H_7N_2)_2[Cu(H_2O)_6](SO_4)_2$ established by O-H···O hydrogen bonds.

Fig. 2: The weak hydrogen bonding between the inorganic entities within the mineral layer of $(C_5H_7N_2)_2[Mn(H_2O)_4(SO_4)_2]$, showing its supramolecular aspect.

Fig. 3: Projection of the structure of $(C_5H_7N_2)_2[Cu(H_2O)_6](SO_4)_2$ and $(C_5H_7N_2)_2[Mn(H_2O)_4(SO_4)_2]$ along the crystallographic a axis, showing the lamellar character and the stacking along the c axis.

Fig. 4: DSC-TG curves for the decomposition of $(C_5H_7N_2)_2[Zn(H_2O)_6](SO_4)_2$ in air.

Fig. 5: VT-PXRD plot of the decomposition of $(C_5H_7N_2)_2[Zn(H_2O)_6](SO_4)_2$.

Fig. 6: DSC-TG curves for the decomposition of $(C_5H_7N_2)_2[Ni(H_2O)_6](SO_4)_2$ in air.

Fig. 7: VT-PXRD plot of the decomposition of $(C_5H_7N_2)_2[Ni(H_2O)_6](SO_4)_2$.

Fig. 8: DSC-TG curves for the decomposition of $(C_5H_7N_2)_2[Cu(H_2O)_6](SO_4)_2$ in air.

Fig. 9: VT-PXRD plot of the decomposition of $(C_5H_7N_2)_2[Cu(H_2O)_6](SO_4)_2$ showing the successive crystalline phases up to $CuSO_4$.

Fig. 10: DSC-TG curves for the decomposition of $(C_5H_7N_2)_2[Co(H_2O)_6](SO_4)_2$ in air.

Fig. 11: DSC-TG curves for the decomposition of $(C_5H_7N_2)_2[Fe(H_2O)_6](SO_4)_2$ in air.

Fig. 12: VT-PXRD plot of the decomposition of $(C_5H_7N_2)_2[Co(H_2O)_6](SO_4)_2$.

Fig. 13: VT-PXRD plot of the decomposition of $(C_5H_7N_2)_2[Fe(H_2O)_6](SO_4)_2$.

Fig. 14: DSC-TG curves for the decomposition of $(C_5H_7N_2)_2[Mn(H_2O)_4\ (SO_4)_2]$ in air.

Fig. 15: VT-PXRD plot of the decomposition of $(C_5H_7N_2)_2[Mn(H_2O)_4\ (SO_4)_2]$.

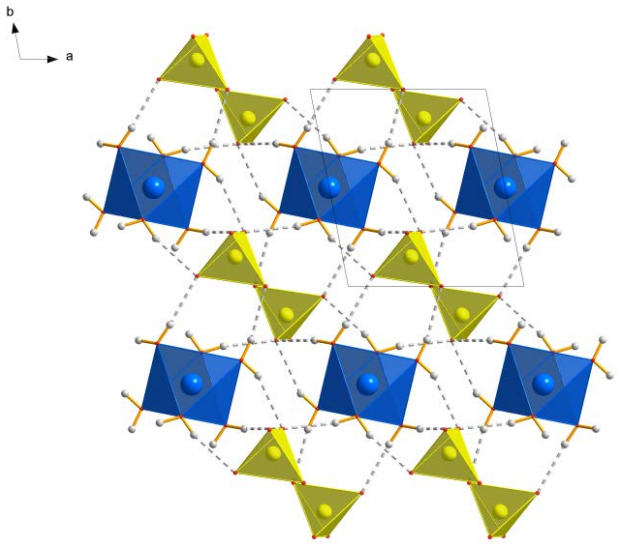

Fig. 1.

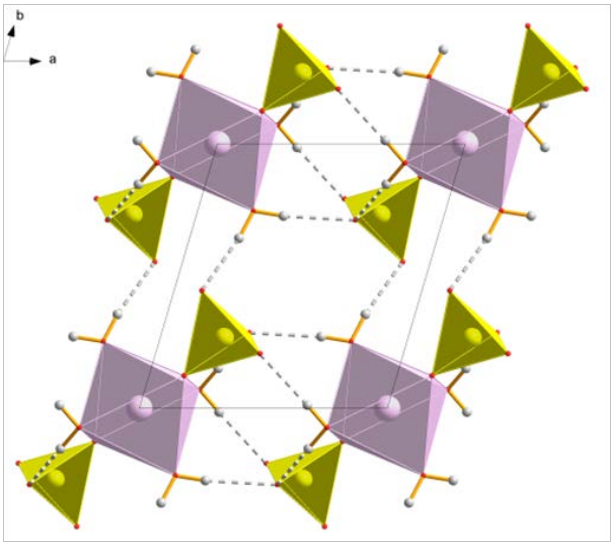

Fig. 2.

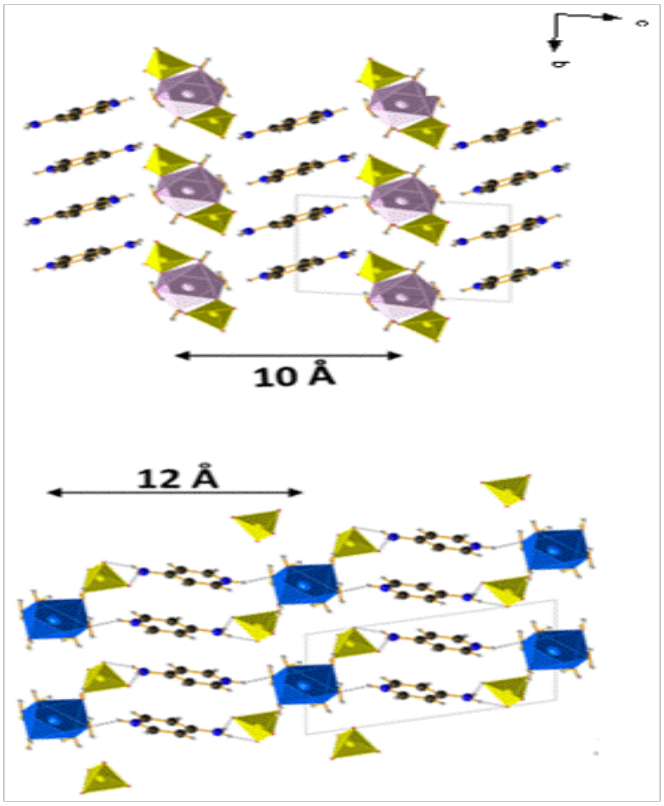

Fig. 3.

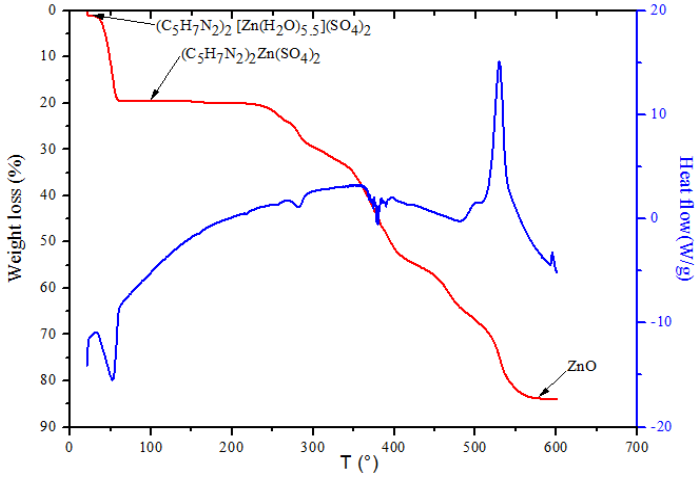

Fig. 4.

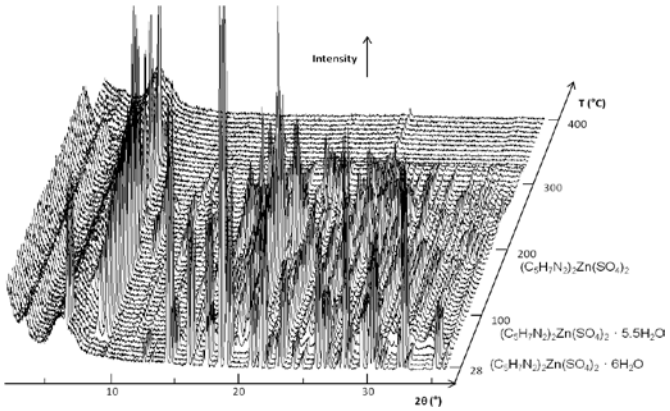

Fig. 5.

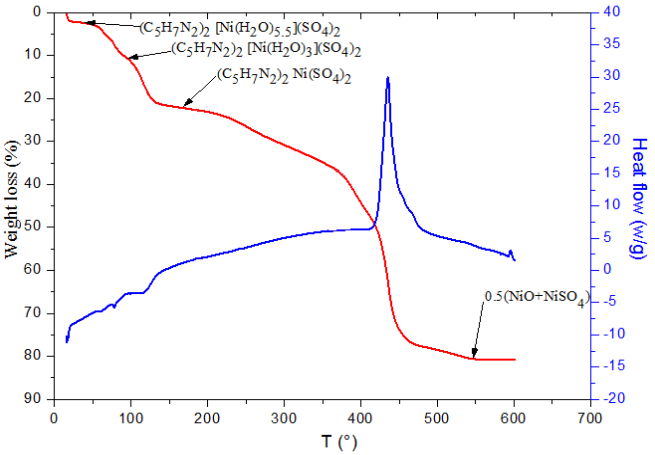

Fig. 6.

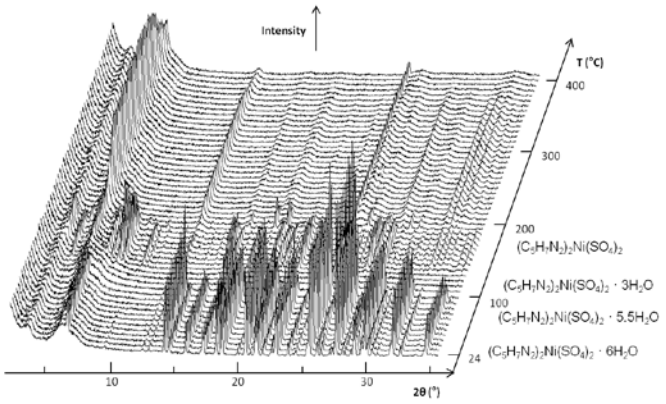

Fig. 7.

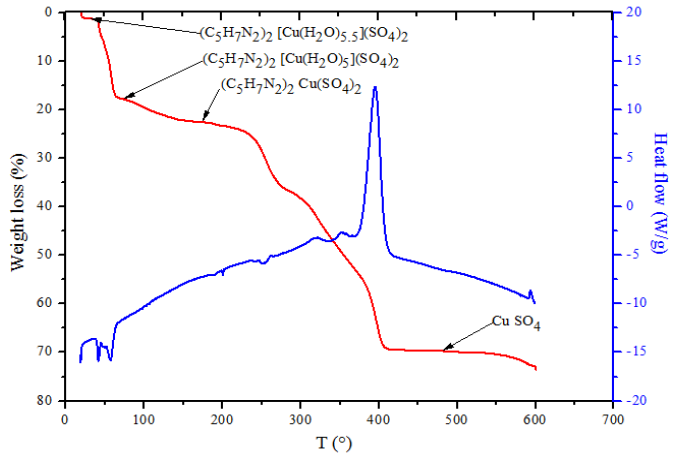

Fig. 8.

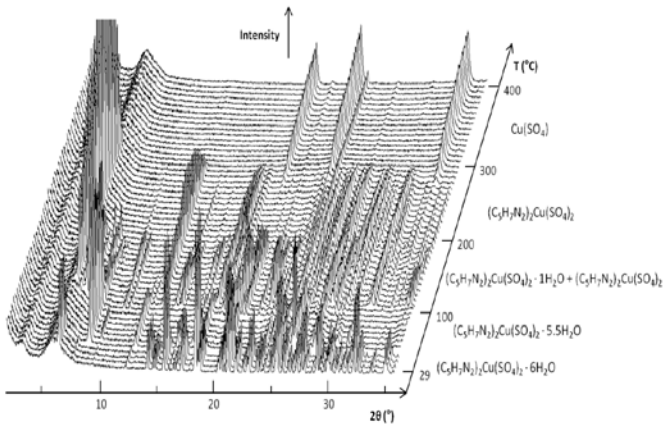

Fig. 9.

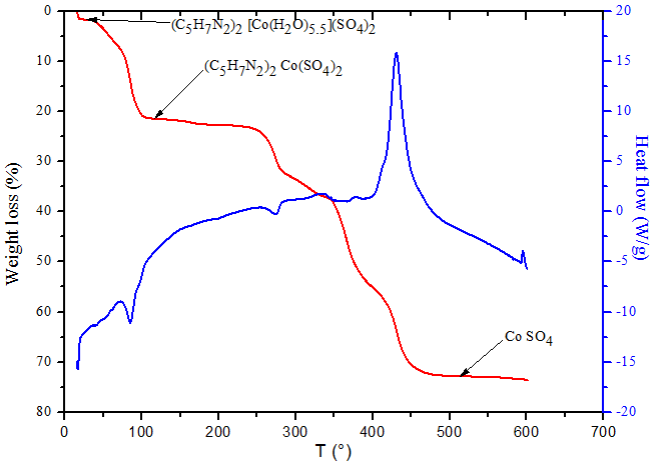

Fig. 10.

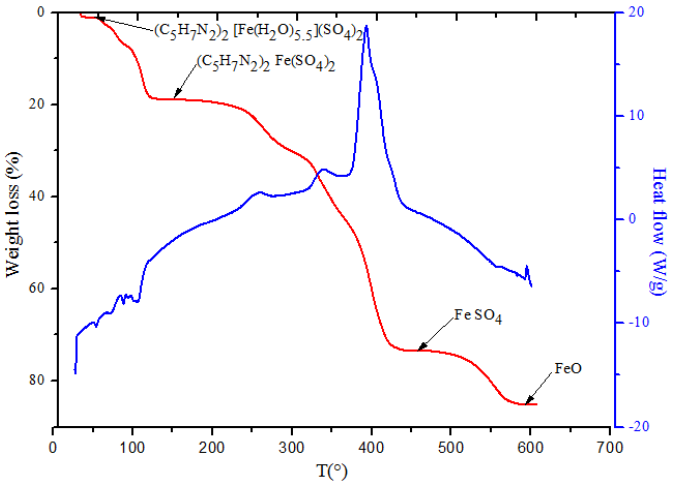

Fig. 11.

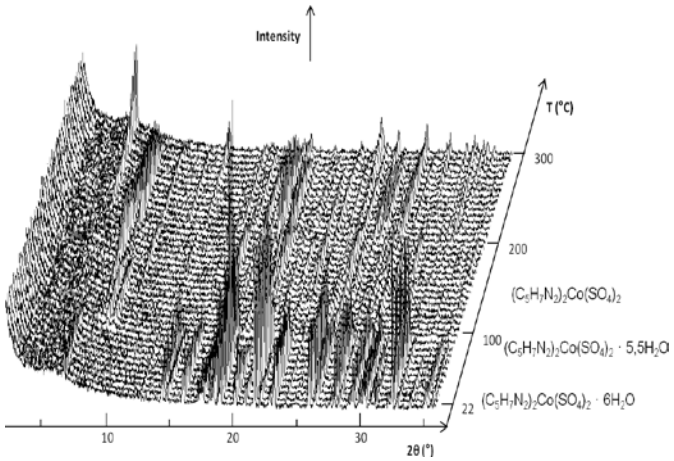

Fig. 12.

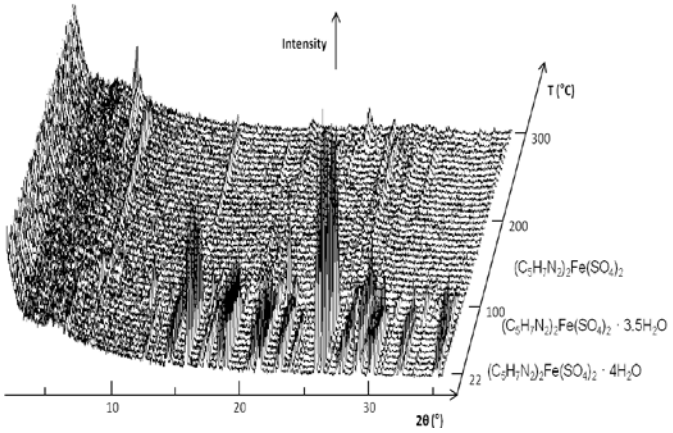

Fig. 13.

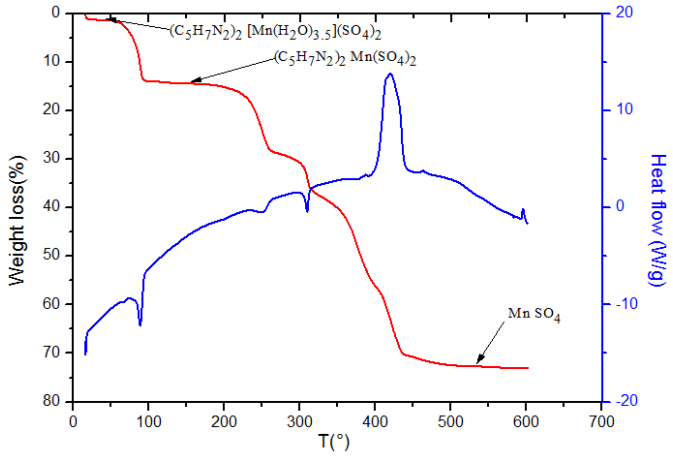

Fig. 14.

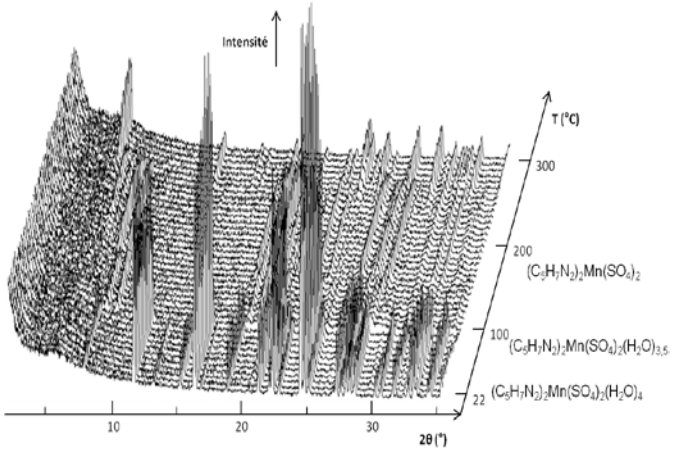

Fig. 15.

Table 1

	MnPRD	CuPRD	CoPRD	NiPRD	FePRD	ZnPRD
interlamellar distance (c parameters) (Å)	10.277	12.369	12.435	12.379	12.530	12.526